



Enhancement mechanism of n-n homojunction δ/α -MnO₂ with fast electron transfer characteristics for efficient photothermal synergistic catalytic oxidation of propane

Yuxi Bi^a, Guoyang Ji^a, Guofei Jiang^b, Chao Feng^c, Yadi Wang^a, Yuekun Jing^a, Yunqi Liu^{a,d}, Huazhen Chang^{e,*}, Fang Liu^{a,d,**}

^a College of Chemistry and Chemical Engineering, China University of Petroleum, Qingdao 266580, China

^b China School of Chemistry and Chemical Engineering, Heze University, Heze 274015, China

^c Key Laboratory of Biofuels, Qingdao Institute of Bioenergy and Bioprocess Technology, Chinese Academy of Sciences, Qingdao 266101, China

^d State Key Laboratory of Heavy Oil Processing, China University of Petroleum, Qingdao 266580, China

^e School of Environment and Natural Resources, Renmin University of China, Beijing 100872, China

ARTICLE INFO

Keywords:

Propane oxidation
Homojunction
Photothermal catalysis
Spatial charge separation
MnO₂

ABSTRACT

The construction of isotype homojunctions composed of the same semiconductor can improve the photo-electrochemical properties, adsorption and catalytic properties of the catalysts, which is important for the enhancement effect in photothermal synergistic catalytic oxidation (PTSCO) system. Herein, a series of homojunctions with δ - and α -phase MnO₂ catalysts were designed and synthesized for propane oxidation in PTSCO system. The δ - α exhibited outstanding propane catalytic oxidation performance ($T_{90} = 198$ °C, $E_a = 20.56$ kJ·mol⁻¹, remarkable water resistance, long-time stability and recycling performance) due to the rich oxygen vacancy, higher low-temperature redox, increased surface acidity, fast transfer and effective separation of photogenerated electron-holes. Additionally, a photothermal synergistic mechanism was proposed based on reaction kinetics, active species detection, density functional theory (DFT) and *in-situ* DRIFTS. This work presents a novel method for the design and preparation of homojunction catalysts. Furthermore, it explains the synergistic mechanism of the PTSCO system.

1. Introduction

Volatile organic compounds (VOCs) are significant contributors to air pollution and can cause irreversible harm to both the ecological environment and human health. [1,2]. The new photothermal synergistic catalytic oxidation technology with the advantages of high solar energy utilization, low activation temperature, high treatment efficiency and low cost is considered to be one of the most promising methods [3–5]. Nevertheless, it is true that the deep catalytic oxidation of saturated alkane VOCs with relatively stable molecular structure and insufficient low-temperature activity has always been a huge challenge to be solved. Propane is a typical light hydrocarbon which is usually used as target pollutant to evaluate the performance of catalysts. It is mainly derived from refineries, various industrial processes, and automobile exhaust [6,7]. Currently, efficient catalysts for the complete

catalytic oxidation of propane include supported noble metal catalysts such as Pt, Pd, and Pb [8]. Nevertheless, noble metal catalysts have several disadvantages that significantly inhibit their practical application, including high cost, poor thermal stability, and susceptibility to poisoning [9]. In contrast, transition metal oxides and their composites have gradually become alternatives to precious metal catalysts due to their low cost, high thermal stability, excellent anti-toxicity, and catalytic oxidation activity [10].

MnO₂ has the advantages of abundant resources, low cost, good environmental compatibility, and high VOCs purification activity, which makes it stand out among many transition metal oxides [11]. However, its narrow band gap and short photogenerated electron-hole lifetime lead to poor photocatalytic performance [12,13]. The construction of homojunctions is an effective strategy to improve the activity of MnO₂ catalysts without relying on additional semiconductors,

* Corresponding author.

** Corresponding author at: College of Chemistry and Chemical Engineering, China University of Petroleum, Qingdao 266580, China.

E-mail addresses: chz@ruc.edu.cn (H. Chang), liufangfw@upc.edu.cn (F. Liu).

<https://doi.org/10.1016/j.apcatb.2024.123920>

Received 1 January 2024; Received in revised form 5 February 2024; Accepted 3 March 2024

Available online 4 March 2024

0926-3373/© 2024 Elsevier B.V. All rights reserved.

which can greatly promote the separation rate of photogenerated electrons and holes and enhances the lifetime of photogenerated carriers, and promote the adsorption, catalysis and photoelectrochemical properties of materials [14–16]. At the interface of the homojunction, a significant number of oxygen vacancies can be generated. This can improve the oxygen mobility and low-temperature reducibility of the catalyst, as well as promote the adsorption and activation of pollutants [17,18]. The performance of the homojunction is also affected by its band structure and distance. Only a homojunction with a suitable band gap can fully utilize the valence and conduction bands to generate $\bullet\text{OH}$ and $\bullet\text{O}^{2-}$, respectively [19]. The Z-type electron transport pathway is considered a superior method for matching band structures [20]. In summary, the homojunction structure can maximize the synergism between photocatalytic and thermal catalytic process by creating interfacial defects and rapidly separating photogenerated electrons and holes. However, the current research on MnO_2 -based homojunctions for environmental regulation is limited and scattered. These studies cover a range of applications, including capacitors, water treatment, microwave absorption, and other fields. However, there is a lack of research on the use of MnO_2 -based homojunctions for the removal of VOCs [21–23]. Moreover, in the photothermal catalytic oxidation system, the effect of homojunction on the deep catalytic oxidation of propane and the related mechanism investigations are even more rarely reported.

Hence, in this study, homojunction $\delta/\alpha\text{-MnO}_2$ nanomaterials were prepared by hydrothermal stirring method, and the structure-activity dependence and synergistic mechanism between homojunction interface characteristics and complete oxidation of propane were explored. Combined with characterization analysis, the deep catalytic oxidation ability influenced by homojunction for propane on homojunction catalysts in photocatalysis oxidation (PCO), thermal oxidation (TCO) and photothermal synergistic catalysis oxidation (PTSCO) systems were evaluated. In addition, with the help of density functional theory (DFT) calculations and *in-situ* DRIFTS, the synergistic mechanism of photothermal catalysis was proposed. This study proposes a novel approach for the design and synthesis of MnO_2 -based homojunction photothermal catalysts and their deep purification of VOCs, and has excellent practical application potential.

2. Experimental

2.1. Synthesis of catalysts

The $\alpha\text{-MnO}_2$ and $\delta/\alpha\text{-MnO}_2$ homojunction catalysts were prepared via enhanced hydrothermal and stirring self-growth method, respectively. The preparation details are described in Text S1, and the scheme is presented in Fig. S1.

2.2. Characterization and theoretical computation of catalysts

A variety of characterization methods were employed to explore the morphology, structure composition, photoelectric and surface property of catalysts. Additionally, *in situ* DRIFTS and DFT were applied to investigate the reaction process. The operation steps for the above characterization techniques and calculations are detailed in Text S2.

2.3. Estimation of photothermal catalytic performance

The evaluation experiment was performed in a self-made closed PTSCO system (Fig. S2). The light source was a 300 W xenon lamp (PLS-SXE 300, Beijing Pfizer), and propane concentration was 2500 ppm (balanced by air). GC-9720 gas chromatography as the detector. The experiment is detailed in Text S3.

3. Results and discussion

3.1. Morphological, crystal and structural characteristics of the catalysts

Fig. 1a1 illustrates that, the nanorods (lines) with loose and rough surface are assembled into a flower-like $\alpha\text{-MnO}_2$ sample, which has a high surface defect rate. Compared with $\alpha\text{-MnO}_2$, the nanosphere boundary of $\delta\text{-MnO}_2$ in Fig. 1b1 is blurred and has a layered nanosheet structure typical of $\delta\text{-MnO}_2$. Fig. S3a1 shows that low content of $\delta\text{-MnO}_2$ essentially unaltered the $\alpha\text{-MnO}_2$ morphological structure when growing δ -phase MnO_2 on the α -phase. With the increase of $\delta\text{-MnO}_2$, the homogeneous structure of $\alpha\text{-MnO}_2$ is gradually formed (Fig. S3b1), but excessive $\delta\text{-MnO}_2$ collapses and slates the homogeneous structure, resulting in different degrees of reduction in both specific surface area and pore volume (Fig. S3c1, d1). Fig. 1c1 displays that $\alpha\text{-MnO}_2$ with a suitable ratios of δ and α phase MnO_2 uniform and complete $\delta/\alpha\text{-MnO}_2$ forms a uniform and complete homojunction structure.

TEM and HRTEM were employed to illustrate the microstructure and crystal plane information of these catalysts. The microstructure corresponding to the SEM results are shown in Fig. 1(a2–c2) and Fig. S3(a2–d2). As can be seen from Fig. 1a3, the main lattice fringe spacing of $\alpha\text{-MnO}_2$ is 6.989 Å, which is related to (110) crystal planes. Fig. 1b3 shows that the main lattice fringe spacing of $\delta\text{-MnO}_2$ are 2.470 Å and 7.040 Å, indicating that the main exposed crystal planes are (110) and (001) crystal surface, respectively. The HRTEM image of 4- δ/α reveals that the lattice spacings of the composites are 6.992 Å, 7.028 Å and 2.482 Å, respectively (Fig. 1c3). These values correspond to the (110) crystal plane of $\alpha\text{-MnO}_2$ and the (110) and (001) crystal planes of $\delta\text{-MnO}_2$, respectively. Fig. S3a3 demonstrates that the composites primarily reveal the (110) crystal plane of $\alpha\text{-MnO}_2$ and the (110) crystal plane of $\delta\text{-MnO}_2$ due to the low concentration of $\delta\text{-MnO}_2$. As the amount of $\delta\text{-MnO}_2$ increases, the (001) crystal plane associated with $\delta\text{-MnO}_2$ gradually emerges (Fig. S3b3–d3). Nonetheless, excessive $\delta\text{-MnO}_2$ can obfuscate the interface boundary of the homojunction and impede the separation of charges by the homojunction catalyst to some extent [19].

Fig. 1d shows that the pure-phase $\alpha\text{-MnO}_2$ catalyst has the characteristic diffraction peaks of tetragonal manganese-type MnO_2 (JCPDS 44–0141) at 2θ of approximately 12.7°, 18.1°, 28.7° and 37.5°, which are attributed to the crystal planes of (110), (200), (310) and (211), respectively. In contrast, the pure-phase $\delta\text{-MnO}_2$ displays the feature peaks of monoclinic- MnO_2 (JCPDS 43–1456), at 2θ about 12.4°, 25.0° and 36.3°, which are associated with the (001), (002) and (110) crystal faces of $\delta\text{-MnO}_2$, respectively. When the δ -phase MnO_2 grows alongside the α -phase, all homogeneous catalysts exhibit the characteristic diffraction peaks of the double crystal phase. However, when $\delta\text{-MnO}_2$ content is low, the (001) crystal plane associated with $\delta\text{-MnO}_2$ is absent, and the spectral peak is narrow at around $2\theta = 12.3^\circ$. Increasing the amount of $\delta\text{-MnO}_2$ results in a wider half-peak width of the diffraction peak. This suggests the appearance of the (001) plane of $\delta\text{-MnO}_2$. Nevertheless, it should be noted that as the $\delta\text{-MnO}_2$ content increase, the peak intensity corresponding to the (110) crystal plane of the homojunction gradually decreases, indicating that the excellent properties belonging to the (110) crystal plane of $\alpha\text{-MnO}_2$ (such as rich oxygen vacancies and excellent low-temperature reduction, etc.) gradually disappear. Therefore, the 4- δ/α homojunction with higher lattice matching has more attractive characteristics.

Fig. 1e illustrates that all samples exhibit a type IV isotherm with a H_3 hysteresis loop in their N_2 adsorption-desorption isotherms. Table 1 presents the specific surface area of catalysts, total pore volume, and average pore size. Pure phase $\delta\text{-MnO}_2$ has the largest specific surface area. While the specific surface area of the homojunction catalysts increase initially and decrease subsequently with the rise in $\delta\text{-MnO}_2$. The 4- δ/α homojunction exhibits the maximum specific surface area ($139 \text{ m}^2\cdot\text{g}^{-1}$) and total pore volume ($0.58 \text{ cm}^3\cdot\text{g}^{-1}$), which is beneficial to expose the active sites favorable for propane catalytic oxidation. However, excessive $\delta\text{-MnO}_2$ can cause material growth to agglomerate,

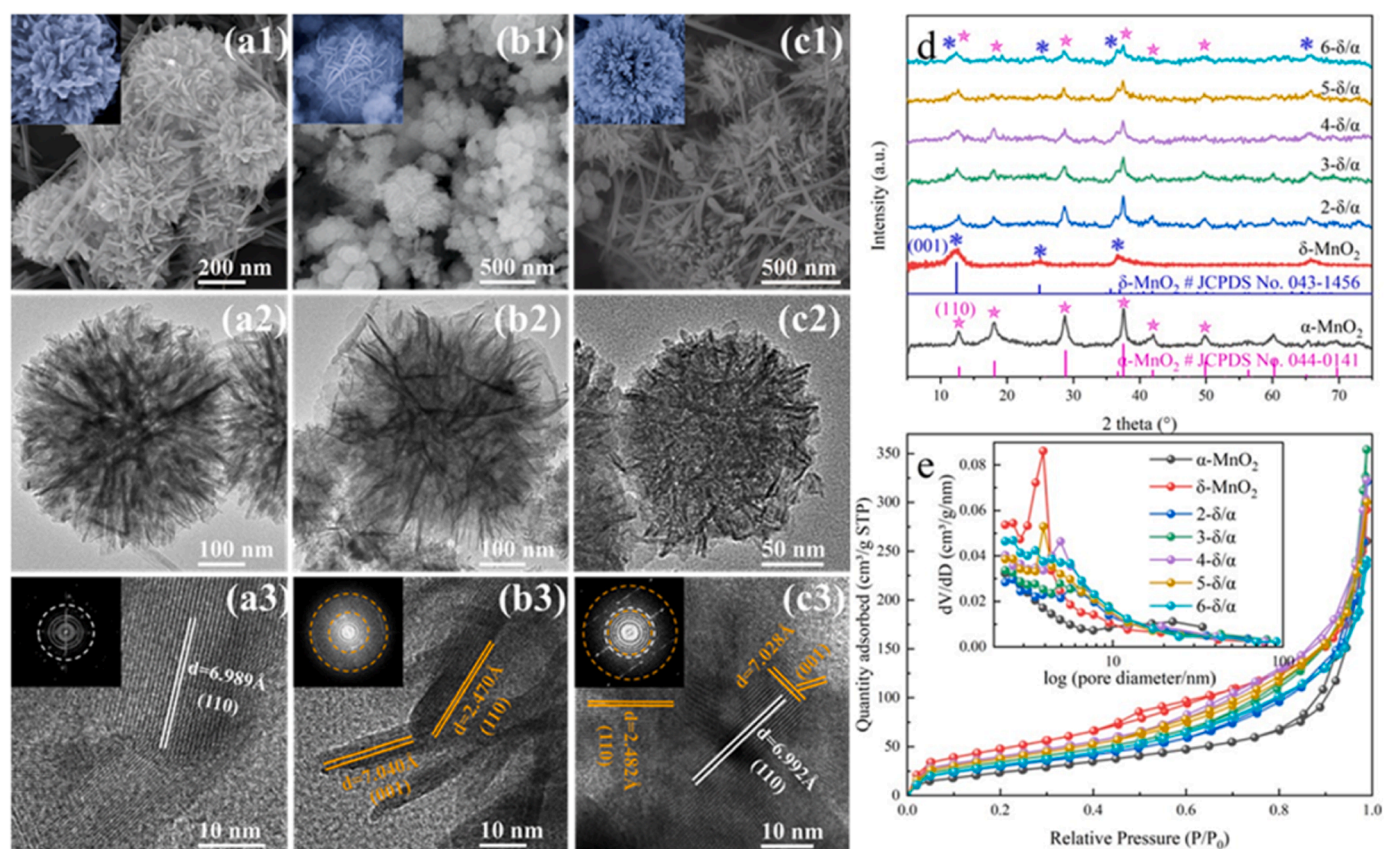


Fig. 1. SEM, TEM and HRTEM images of (a1-a3) α -MnO₂, (b1-b3) δ -MnO₂ and (c1-c3) 4- δ/α , (d) XRD patterns and (e) N₂ adsorption-desorption isotherms of α -MnO₂, δ -MnO₂, 2- δ/α , 3- δ/α , 4- δ/α , 5- δ/α and 6- δ/α catalysts.

Table 1

Parameters of the physical structure and surface chemical composition of catalysts.

Catalysts	S_{BET} (m ² ·g ⁻¹)	Total pore volume (cm ³ ·g ⁻¹)	Average pore size (nm)	XPS			
				Mn ³⁺ +Mn ²⁺ /Mn ⁴⁺ (%)	V _O (%)	O _{OH} +O _{ads} /O _{lat} . (%)	AOS
α -MnO ₂	101	0.34	4.52	2.95	31.05	47	3.39
δ -MnO ₂	166	0.45	3.37	2.56	20.24	42	3.43
3- δ/α	104	0.50	4.76	3.63	34.05	46	3.21
2- δ/α	120	0.51	4.26	4.07	35.33	61	3.17
4- δ/α	139	0.58	5.13	4.91	36.62	68	3.03
5- δ/α	124	0.46	3.56	3.24	32.42	49	3.23
6- δ/α	89	0.41	3.16	2.81	30.47	43	3.41

leading to severe adherence of the homojunction structure.

3.2. Catalytic oxidation activity of propane

The performance of heterojunction catalytic oxidation has been evaluated in PCO, TCO, and PTSCO systems. Fig. S4 suggests that, in PCO system, none of the catalysts can degrade propane solely under light conditions. Interestingly, in TCO system, all catalysts show improved propane degradation activity (Fig. 2a), and the order of activity is as follows: 4- δ/α > 3- δ/α > 2- δ/α > 5- δ/α > α -MnO₂ > 6- δ/α > δ -MnO₂. Fig. 2b shows that 4- δ/α has the lowest activation energy (33.85 kJ·mol⁻¹), implying that the rate-determining step can be carried out more easily. Additionally, TOF (calculated by CO-TPD, Fig. S5) is a characteristic index to evaluate the intrinsic performance of the catalyst. As shown in Fig. 2c, 4- δ/α displays the highest TOF. Furthermore, the reaction rate (r, Fig. S6a), as well as the specific surface activity (SSA, Fig. S6b) reconfirm the charming oxidation capacity of 4- δ/α . Table S1 summarizes the relevant parameters of propane degradation activity for

different catalysts in the TCO system. As well as, Table S2 compares the activity of catalysts with other studies, the 4- δ/α prepared in this study has excellent catalytic oxidation of propane activity. Dramatically, propane decomposition activity is significantly enhanced within the PTSCO system and the 4- δ/α still exhibits the highest propane degradation capacity (Figs. 2d, S6c, S6d). Fig. 2e displays that the apparent activation energy (E_a) of the reaction of catalyst 4- δ/α in the PTSCO system continues to decrease to 20.56 kJ·mol⁻¹. In addition, the introduction of light improve the reaction rate of the catalysts (Fig. 2f). In comparison to the PCO and TCO systems, the PTSCO system demonstrates a significantly enhanced ability to degrade propane and reaction rate. Table S3 presents the relevant parameters for propane degradation in the PTSCO system.

Propane degradation tests were performed to examine the synergistic effect of light and thermal in the PTSCO system. The tests were conducted on 4- δ/α in PCO, TCO, and PTSCO systems, respectively. Fig. 3a indicates that 4- δ/α has a negligible propane degradation under only light irradiation. Compared with TCO system, the conversion rate of

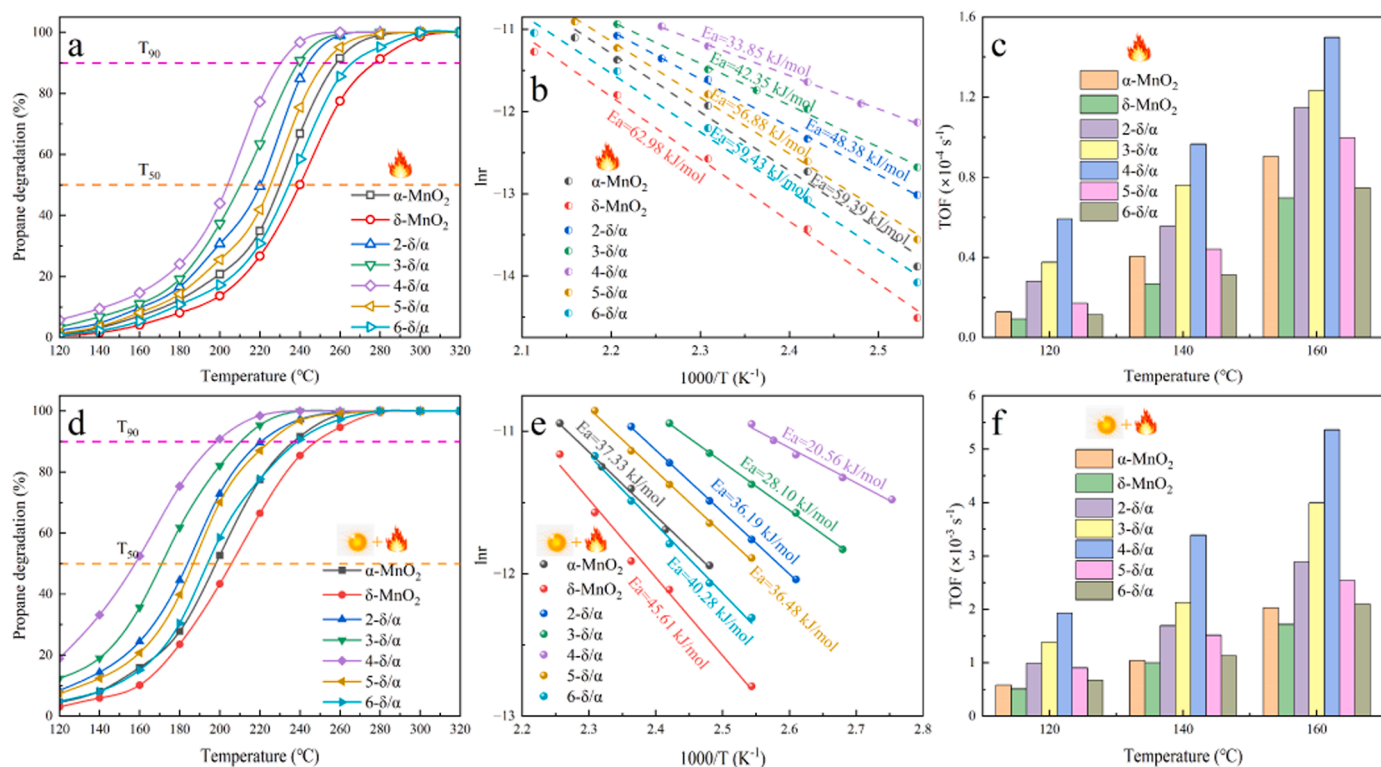


Fig. 2. (a), (d) Degradation activity of propane and (b), (e) the Arrhenius plots corresponding to conversions below 20%, and (c), (f) TOF in TCO and PTSCO systems, respectively. (Reaction conditions: the catalyst used was 0.2 g and the concentration of propane was 2500 ppm, balanced with air, and the WHSV was 30000 mL·g_{cat}⁻¹·h⁻¹).

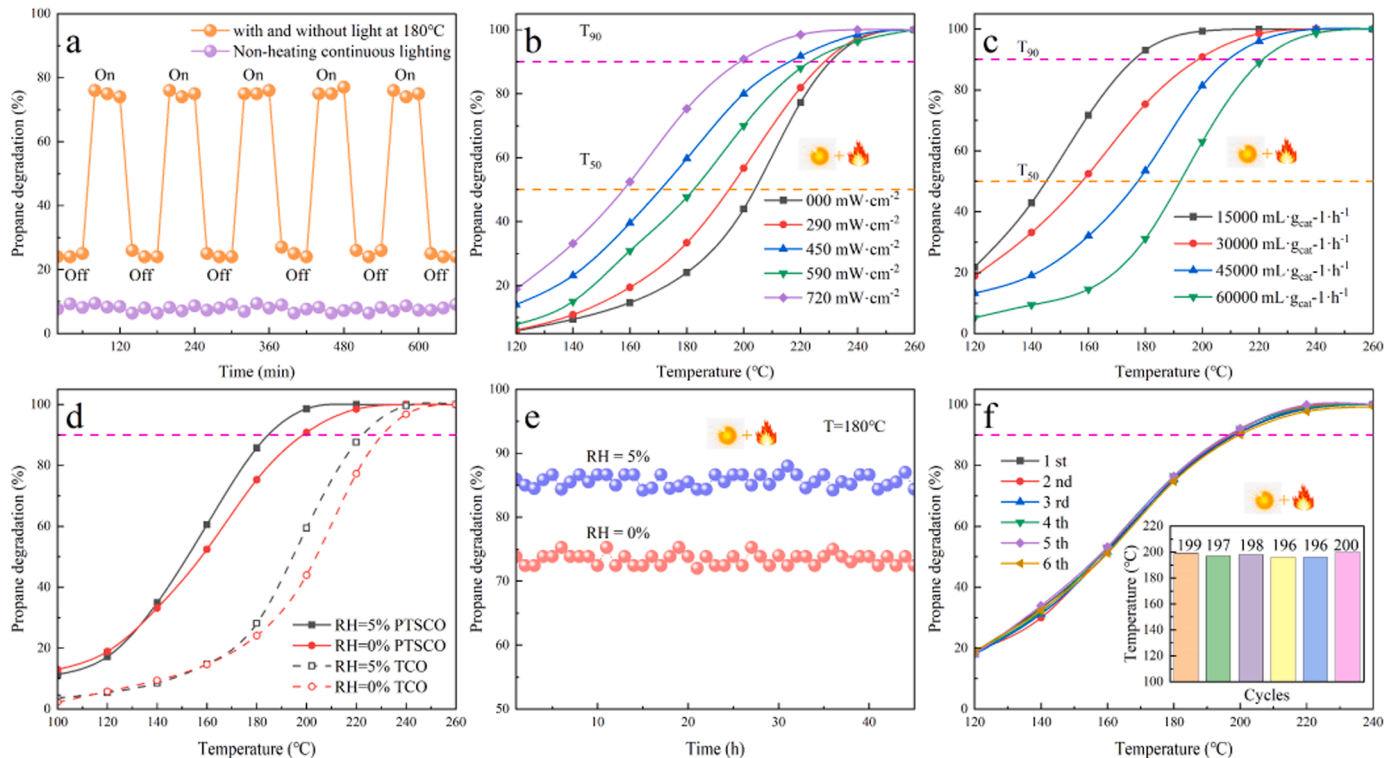


Fig. 3. Propane degradation over the 4- δ/α catalyst in various conditions: (a) with and without light at 180°C and only continuous irradiation, the effects of (b) different irradiation intensity, (c) disparate WHSV and (d) 5 vol% water, (e) longstanding stability under dry and humid and (f) recycling performance. (Reaction conditions: the catalyst used was 0.2 g and the concentration of propane was 2500 ppm, balanced with air).

propane increases significantly under light on (PTSCO system), and the light enhancement process was repeatable. Therefore, it is the synergistic effect of light and heat that accounts for the exceptional performance of the 4- δ/α catalyst in the degradation of propane.

The propane catalytic oxidation ability of 4- δ/α under different light intensities controlled by adjusting the current in the PTSCO system was tested (Fig. 3b). The 4- δ/α catalyst exhibits optimal photothermal activity for propane at a light intensity of $720 \text{ mW}\cdot\text{cm}^{-2}$, revealing that the photoinduced excitation promotes the generation of stimulated hole-

electron pairs [24]. Additionally, it has been indicated that higher light intensity is advantageous for the release of active centers and the generation of reactive oxygen species.

Fig. 3c illustrates the impact of WHSV on the removal of propane using the 4- δ/α catalyst. The increase of WHSV is accompanied with a higher light-off temperature and a lower propane degradation. The T_{90} of 4- δ/α at various conditions, including 15000, 30000, 45000 and 60000 $\text{mL}\cdot\text{g}_{\text{cat}}^{-1}\cdot\text{h}^{-1}$, is noted at 176°C , 195°C , 209°C and 221°C , correspondingly. Propane has insufficient contact with the catalyst when the

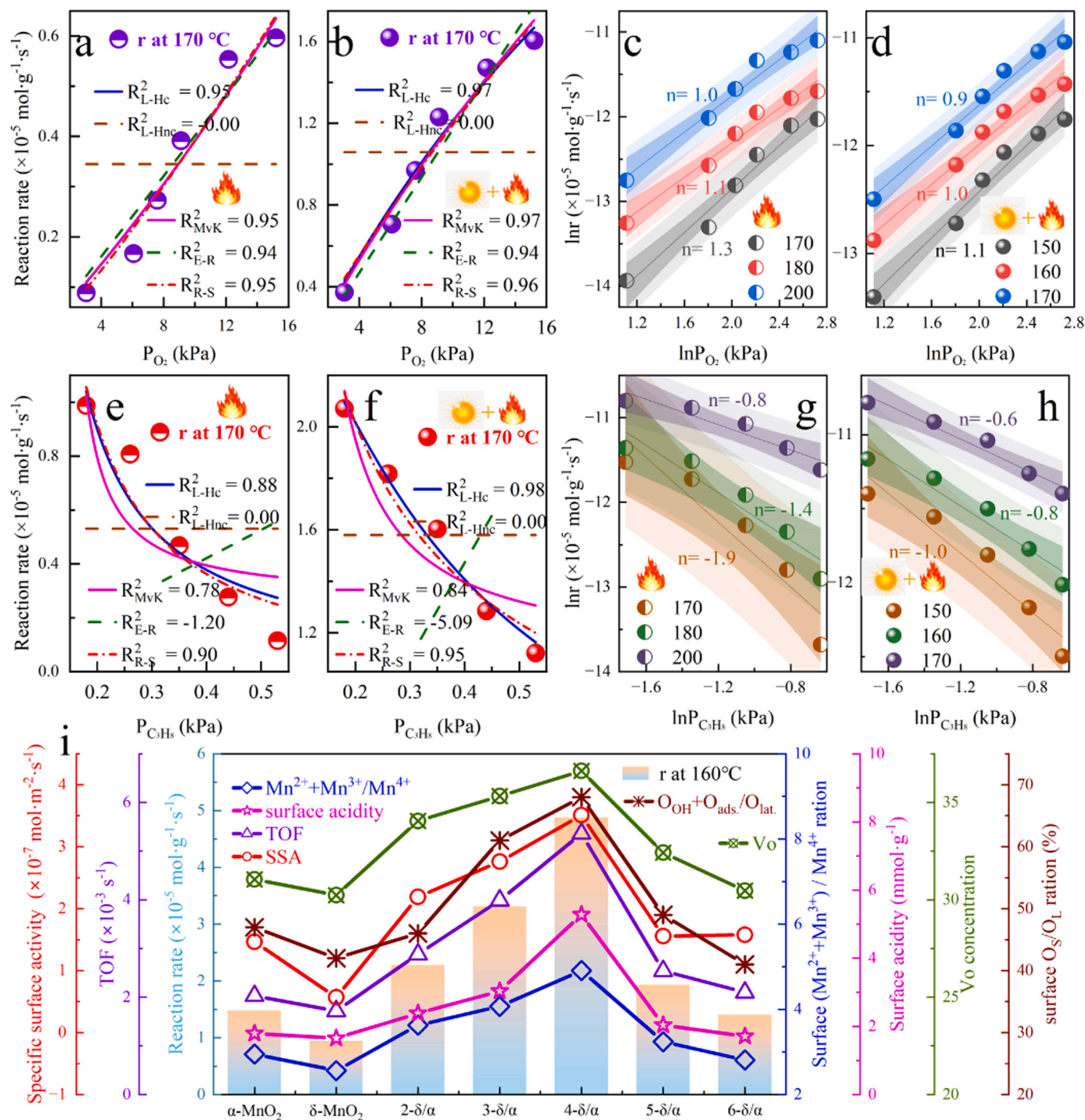


Fig. 4. (a) Kinetic models fitting curves of multiple models and the dependence of the reaction rate for propane oxidation over 4- δ/α catalytic on the partial pressure of (a, b, c, d) propane and (e, f, g, h) O_2 in TCO and PTSCO system, (i) the structure-activity relationship of reaction rate (r) and the molar ratio of $(\text{Mn}^{2+}+\text{Mn}^{3+})/\text{Mn}^{4+}$, surface acidity, specific surface activity (SSA), TOF, $\text{O}_{\text{OH}}+\text{O}_{\text{ads}}/\text{O}_{\text{lat}}$, and V_O . (Reaction conditions: the catalyst used was 0.2 g; the fixed partial pressure of propane in (a-d) is 0.40 kPa and O_2 in (e-h) is 9.31 kPa, and the WHSV was $30000 \text{ mL}\cdot\text{g}_{\text{cat}}^{-1}\cdot\text{h}^{-1}$).

WHSV is high, leading to a shorter residence time on the catalyst surface. Importantly, the catalyst can still maintain excellent catalytic performance at high WHSV.

Generally, during the degradation of VOCs, water can competitively occupy the adsorption sites of the catalyst, inhibiting the adsorption and stimulation of propane on the catalyst surface, ultimately reducing catalyst's activity. However, it is worth noting that the activity of propane oxidation in both TCO and PTSCO actually increases with increasing humidity (Fig. 3d, S7a, S7b), despite common perceptions. Therefore, combined with subsequent analysis, it can be inferred that water vapor is converted into active species (hydroxyl radical) during the degradation of propane. Furthermore, it is evident from the data presented in Fig. S7c that the E_a of the PTSCO system under humid conditions ($21.45 \text{ kJ}\cdot\text{mol}^{-1}$) is lower than that of the dry PTCO system ($23.89 \text{ kJ}\cdot\text{mol}^{-1}$), indicating that the [25] that the timely consumption of water vapor in the products or the intake air enhances the water resistance of the catalysts.

In order to examine the stability of $4\text{-}\delta/\alpha$ while switching between high and low temperatures, the study employed two distinct temperatures: 300°C and 180°C . Fig. S8 shows the excellent stability of $4\text{-}\delta/\alpha$, and the propane degradation efficiency can still be maintained even after six cycles. Additionally, Fig. 3e illustrates the prolonged catalytic stability of the $4\text{-}\delta/\alpha$ catalyst at 180°C under dry and 5% humidity, indicating exceptional durability even in humid conditions. The cycle stability test of the catalyst is shown in Fig. 3f. After 6 cycles, no significant change in the catalytic activity of A catalyst is observed, and the T_{90} values of the first to sixth cycles were 199°C , 197°C , 198°C , 196°C , 196°C and 200°C , respectively. The above results indicate that the $4\text{-}\delta/\alpha$ catalyst has excellent structural stability and satisfactory cycle and long-term stability even under humid conditions.

3.3. Kinetics and structure-activity relationship

In order to clarify the kinetics of propane catalytic oxidation process, the correlation between the reaction rate of $4\text{-}\delta/\alpha$ and the partial pressure of O_2 and C_3H_8 under different conditions was determined by using various models (Text S4). At the identical temperature, an increase in partial pressure of propane results in a gradual decrease in catalytic activity and reaction rate of the $4\text{-}\delta/\alpha$ catalyst. Figs. 4a, 4b displays the outcomes of fitting diverse kinetic models at a temperature of 170°C . Excluding subjective evaluations, the L-H_{nc} (Non-competitive) model are unsuitable for this investigation, as their fitting correlation coefficient (R^2) is negative. The remaining three models' sequence is as follows: L-H competitive model = MvK model \geq P-S model $>$ E-R model. Markly, the R^2 of all the models are greater than 94%, revealing that the degradation process of propane in the PTSCO system is controlled by a variety of models under low temperature and oxygen enrichment. In particular, Fig. 4a, b show that the introduce of light has little effect on the fitting results of the reaction kinetic, when the propane partial pressure was fixed. This may be due to an excess of O_2 gas. The results can be further confirmed by the reaction order in Fig. 4c, d. In both TCO and PTSCO systems, the n value of O_2 is only slightly reduced by increasing temperature or increasing light. While, when the O_2 partial pressure is fixed, the kinetic fitting curves show different results. Fig. 4e indicates that, in TCO system, the fitted model of L-H_{nc} and E-R are unfitting this investigation due to the negative correlation coefficient. In addition, the correlations from large to small are: L-H competitive model $>$ R-S model $>$ MvK model. This demonstrates that both P-S and L-H competition models are effective in describing the degradation process of propane within the TCO system. Interestingly, in the PTSCO system (Fig. 4f), the correlation constants (R^2) of the fitting curves increase, suggesting the stronger dependence with propane partial pressure. However, the P-S and L-H competition models are still not applicable. Furthermore, Fig. 4g demonstrates that in the absence of light, the value of n for propane gradually increases with rising temperature. This suggests that higher temperatures promote the adsorption of propane over

the catalyst. More importantly, the introduction of light in PTSCO system results in an increase in the n value of propane to -0.6 (Fig. 4h), indicating that more C_3H_8 can reach the catalyst interface and be activated. The above results show that photothermal catalysis can accelerate the rate-determining step of the oxidation reaction by improving the accessibility of C_3H_8 molecules [26].

Fig. 4i reveals the structure-activity relationship between $4\text{-}\delta/\alpha$ and propane oxidation. The findings reveal that there is a positive relationship between the ratio and the propane degradation activity. The larger molar proportion of $(\text{Mn}^{2+} + \text{Mn}^{3+})/\text{Mn}^{4+}$ indicates the more unsaturated coordination bonds, which results in the stronger redox capacity [27]. The reaction rate is also well correlated with TOF, surface acidity, SSA and $\text{O}_{\text{OH}} + \text{O}_{\text{ads.}}/\text{O}_{\text{lat.}}$.

3.4. Photothermal synergistic effect

3.4.1. Chemical properties and defects on the catalysts surface

XPS is employed to explore the chemical states of different elements in the catalysts. Fig. 5a presents the Mn 2p XPS spectra of all samples, which can be identified as three characteristic peaks at the binding energies of approximately 640.9 eV, 642.1 eV and 643.5 eV. These peaks correspond to Mn^{2+} , Mn^{3+} and Mn^{4+} species, respectively. Based on the area of XPS peak, the $(\text{Mn}^{2+} + \text{Mn}^{3+})/\text{Mn}^{4+}$ proportion and oxygen vacancy (Vo , $\text{Vo} = (1 - (2[\text{Mn}^{2+}] + 3[\text{Mn}^{3+}] + 4[\text{Mn}^{4+}])/4) \times 100\%$) are further explored and summarized (Table 1). Typically, a higher concentration of low-valence Mn (Mn^{2+} , Mn^{3+}) facilitates the acceleration of oxygen activation and dissociation in the surrounding area. This leads to a significant weakening of the Mn-O bond and the creation of numerous oxygen vacancies.[28,29]. In addition, as illustrated in Table 1, the average oxidation state (AOS) values of manganese obtained from Mn 3 s (Fig. 5b) of the catalysts is arranged as follows: $4\text{-}\delta/\alpha < 3\text{-}\delta/\alpha < 2\text{-}\delta/\alpha < 5\text{-}\delta/\alpha < \alpha\text{-MnO}_2 < 6\text{-}\delta/\alpha < \delta\text{-MnO}_2$.

The XPS for O1s in Fig. 5c demonstrates that spectral peaks corresponding to the surface hydroxyl group (labelled as O_{OH} , from water or hydroxyl groups), surface adsorbed oxygen (labelled as $\text{O}_{\text{ads.}}$, from water), and lattice oxygen (labelled as $\text{O}_{\text{lat.}}$, from water) of the catalyst emerge at binding energies of 532.8 eV, 531.7 eV, and 530.0 eV, respectively[30]. Fig. 3c and Table 1 illustrate that $4\text{-}\delta/\alpha$ has the highest Vo content, which implies that it possesses the densest reaction sites [31]. Compared with other catalysts, the $\text{O}_{\text{lat.}}$ of $4\text{-}\delta/\alpha$ shifts slightly towards a lower binding energy, indicating a weaker Mn-O interaction, which is consistent with the results of Raman spectroscopy. This is due to the fact that the presence of oxygen vacancies increases the electron density of lattice oxygen, thereby reducing the binding energy of lattice oxygen.

The EPR is used to detect the oxygen vacancy content of the sample, and the results are shown in Fig. 5d. For homojunctions, the signal intensity of electron spin resonance (EPR) initially rises and then falls with an increase in δ -phase MnO_2 , peaking at $4\text{-}\delta/\alpha$. Notably, despite its strong oxygen vacancy signal, monomeric $\delta\text{-MnO}_2$ shows a low catalytic activity for propane oxidation. On the one hand, combined with Raman spectroscopy and XPS tests, it can be seen that it is likely that bulk oxygen vacancies occupy the majority[32]. On the other hand, excessive oxygen vacancies causing an imbalance of Mn ions in the lattice and an increase in adsorption sites on the catalyst surface leads to an inoperative effect to the catalytic oxidation performance. Compared to room temperature, the Vo of all catalysts increase rapidly at 220°C , with $4\text{-}\delta/\alpha$ having the highest concentration. This suggests that heating accelerates the molecular motion of adsorbed oxygen, subsurface or bulk lattice oxygen on the catalyst surface, leading to the formation of more oxygen vacancies[33].

In broad terms, the transformation in MnO_2 crystal structure is found on the $[\text{MnO}_6]$ octahedral unit [34]. Specifically, in the Raman spectra of $\alpha\text{-MnO}_2$ (Fig. 5e1), the bands at $630\text{--}645 \text{ cm}^{-1}$ and $560\text{--}575 \text{ cm}^{-1}$ are attributed to the ν_2 symmetric stretching vibration of Mn-O perpendicular to the $[\text{MnO}_6]$ octahedral double chain direction

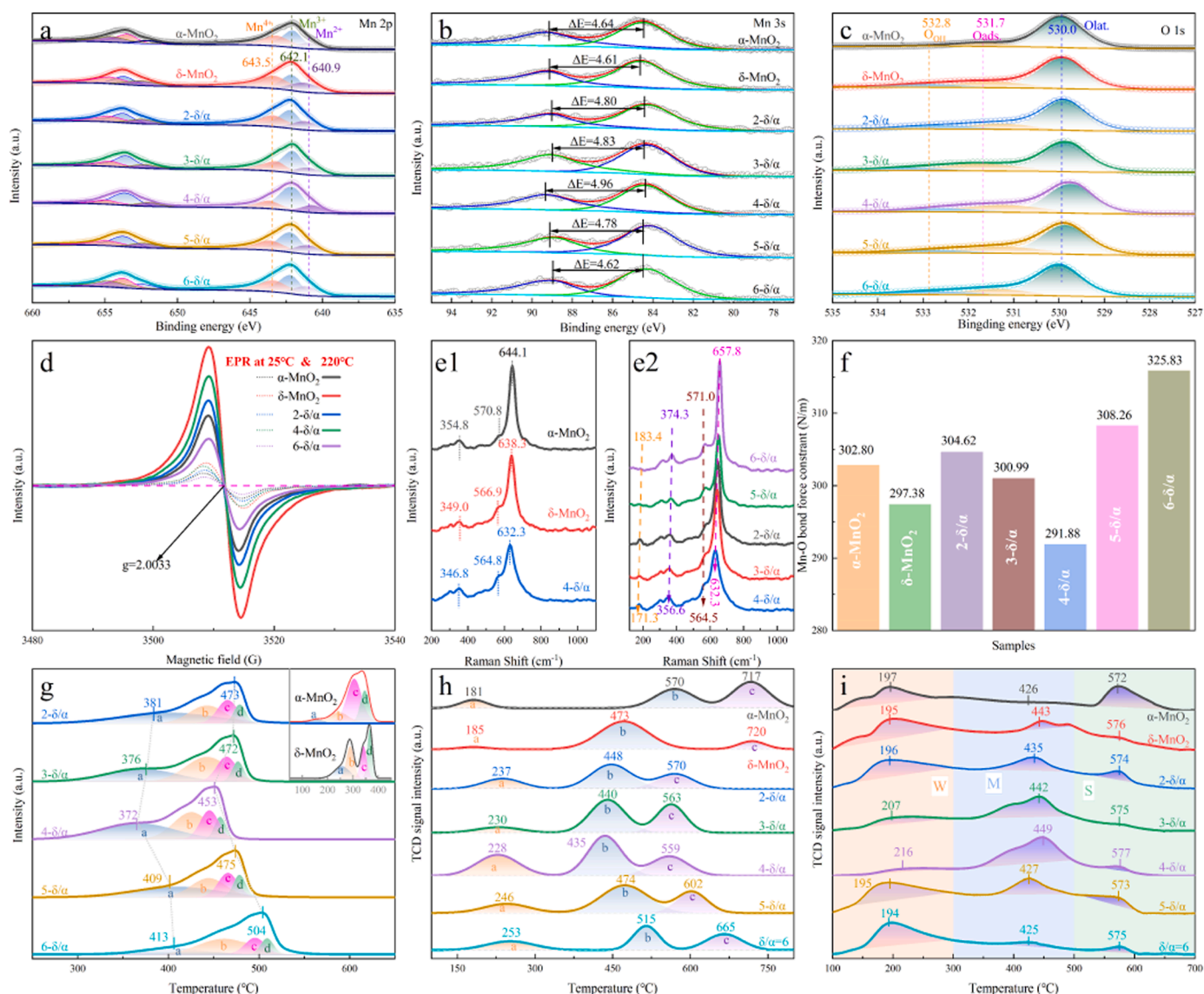


Fig. 5. XPS spectra of (a) Mn 2p, (b) Mn 3s, (c) O 1s, (d) EPR spectra at room temperature and 220°C, (e) Raman spectra patterns, (f) M-O bond strength constant, (g) H₂-TPR profiles, (h) O₂-TPD profiles and (i) NH₃-TPD profiles of α -MnO₂, δ -MnO₂, 2- δ/α , 3- δ/α , 4- δ/α , 5- δ/α and 6- δ/α catalysts.

and the ν_3 stretching vibration of oxygen relative to the manganese along the [MnO₆] octahedral double chain direction, respectively. Furthermore, the Raman peaks at 360 cm⁻¹ and 180 cm⁻¹ are attributed to the bending vibration of Mn-O at the shared angle position and the translational motion of the [MnO₆] octahedron, respectively [35]. On the contrary, the δ -MnO₂ exhibits an incomplete crystal structure, and there are more surface mismatches resulting in the Raman spectra moving slightly to low wavenumbers [36]. Obviously, when homojunctions are prepared by uniformly loading the δ -phase MnO₂ onto the α -phase, it can be seen that the Raman peak intensity of the 4- δ/α sample is weakened, the half-peak width becomes broader and there is a certain degree of redshift, suggesting that the formation of homojunctions distorts the crystal structure of the pure phases of α - and δ -MnO₂, which facilitates the generation of oxygen vacancies [37,38]. Fig. 5e2 indicates that with the increase of δ -MnO₂, the crystal structure of the homojunction varies from having more defects to being progressively more complete. For 4- δ/α , the intensity of the peak at 632.3 cm⁻¹ is the smallest and the width is the widest, which corresponds to the XRD results.

Raman spectroscopy can be used to determine the force constant (k) of the M-O bond according to Hooke's law (Text S5). As illustrated in

Fig. 5f, the k values of the prepared samples were in descending order: 6- δ/α > 5- δ/α > 2- δ/α > α -MnO₂ > 3- δ/α > δ -MnO₂ > 4- δ/α , which is basically in agreement with their photo-thermal catalytic oxidative activity towards propane degradation activity. This is because the weaker the vibration intensity of the Mn-O bond, the easier the Mn-O breaks, which promotes the reactivity of the surface lattice oxygen, leading to an increase in the mobility and redox properties of the reactive oxygen species [39].

The reduction capacity of the samples and the catalytic activity of active oxygen species can be investigated by H₂-TPR. As demonstrates in Fig. 5g, four reduction peaks can be identified in the temperature range of 380–420°C and 450–500°C. The peak 'a' corresponds to the activity of surface active groups, such as O₂ and O₂⁻. Meanwhile, the peaks 'b', 'c' and 'd' correspond to the gradual reduction process of MnO₂ to Mn₂O₃, Mn₂O₃ to Mn₃O₄ and Mn₃O₄ to MnO, consecutively [40]. Compared with the monomer α -MnO₂ and δ -MnO₂, the reduction peak temperatures of all homojunction catalysts move to higher temperatures, suggesting the presence of strong interaction and the successful formation of heterojunction interface between α - and δ - phase MnO₂ in the homojunction. Furthermore, higher reduction temperatures may signify that the catalyst has a higher concentration of surface oxygen

vacancies[41]. For all homojunction catalysts, 4- δ/α exhibits the lowest reduction peak temperature of surface adsorption oxygen. It indicates that both its surface and bulk phase lattice oxygen possess higher oxygen mobility and rich defect sites, which is consistent with Raman spectroscopy [42]. Furthermore, Table S4 illustrates the consumption of H_2 in the reduction process. All catalysts exhibit the H_2 consumption below the theoretical values, implying that there is a certain amount of Mn^{3+} or Mn^{2+} which benefits the generation of Vo in the samples.

On the other hand, the oxygen species types of the samples were further analyzed by O_2 -TPD. As shown in Fig. 5h displays three distinct O_2 desorption peaks in all samples. These peaks represent the transformation of adsorbed oxygen and surface-active oxygen (O_{ads}) at low-temperature, subsurface lattice oxygen (O_{sur}) at middle-temperature, and bulk lattice oxygen (O_{lat}) at high-temperature, respectively [43]. The α - MnO_2 and δ - MnO_2 catalysts present the lowest surface adsorbed oxygen release temperature of approximately 180 °C, although their propane degradation activity is not the most efficient. This indicates that in addition to temperature, the content of surface adsorbed oxygen and lattice oxygen is also an important factor affecting the performance of the catalyst [44]. Table S5 indicate that 4- δ/α has high mobility and abundant content of oxygen species at low temperature. This finding is consistent with the H_2 -TPR results.

It is generally believed that the acidic sites on catalyst's surface are conducive to the adsorption of VOCs and the activation of C-H bonds, which makes the reaction more inclined to deep oxidation [45]. The NH_3 -TPD curves depicted in Fig. 5i present that all catalysts have three types of acid sites, namely, weak acid sites related to surface hydroxyl groups at 100–300 °C, medium acid sites associated with weak Brønsted acid sites at 300–500 °C and strong acid sites linked to strong Brønsted acid sites and Lewis acid sites at 500–700 °C [46,47]. In certain instances, the enhancement of acid sites possessing medium strength may accelerate the catalytic oxidation proficiency of propane [48]. Compared to other samples, the 4- δ/α catalyst exhibits a higher temperature of acid site as well as larger intensity of peaks, indicating stronger acidity and richer acid centers in the medium-strong acid range.

Meanwhile, Table S6 reveals that 4- δ/α possesses the most number of acidic sites that can promote the adsorption of propane molecules [49].

3.4.2. Optical properties and band gap structure of catalysts

In order to explore the unique band structure of the x- δ/α homojunction, the UV–visible spectra of the samples were analyzed, and the outcomes are presented in Fig. 6a. Due to the black nature of the composites, all samples exhibit comparable light absorption capacity throughout the entire spectral range. Furthermore, there is a rise in the absorbance of the 4- δ/α catalyst in the visible region. The band gap energies (E_g) of α - MnO_2 and δ - MnO_2 calculated by Tauc plot method are 2.09 eV and 2.46 eV, respectively (the inset in Fig. 6a). Furthermore, the direction of electron transfer in photogenerated carriers was further investigated by Mott-Schottky spectroscopy. It is evident from Fig. S9 that both α - MnO_2 and δ - MnO_2 are n-type semiconductors as indicated by their positive slopes. Therefore, the conduction band (E_{CB}) and the valence bands (E_{VB}) are -0.83 V and 1.26 V, -0.35 V and 2.11 V (vs. NHE), respectively. Furthermore, the E_{VB} values of α - MnO_2 (1.20 eV) and δ - MnO_2 (2.09 eV) obtained from XPS valence band spectra (Fig. S10) are basically consistent with the calculated valence bands.

The separation efficiency of photogenerated electron-hole pairs of the prepared samples was analyzed by photoluminescence (PL) spectroscopy, transient photocurrent response and electrochemical impedance spectroscopy (EIS). Fig. 6b displays the results of the transient photocurrent response of the samples. It can be clearly seen that the sequence of its intensity goes as follows: 4- δ/α > 3- δ/α > 2- δ/α > 5- δ/α > α - MnO_2 > 6- δ/α > δ - MnO_2 , implying a substantial enhancement in electron-hole transfer at the composite interface[50]. Additionally, the photocurrent response intensity of the homojunction catalysts initially increase and then decrease with an increase in δ - MnO_2 , indicating that the formation of the homojunction structure is influenced by the ratio of δ - MnO_2 and α - MnO_2 . As indicated in Fig. 6c, the PL intensity of 4- δ/α is weakest, inferring that the successful construction of δ - MnO_2 and α - MnO_2 homojunctions has effectively promoted the separation ability of photogenerated electron and hole pairs. The EIS in Fig. 6d, used to

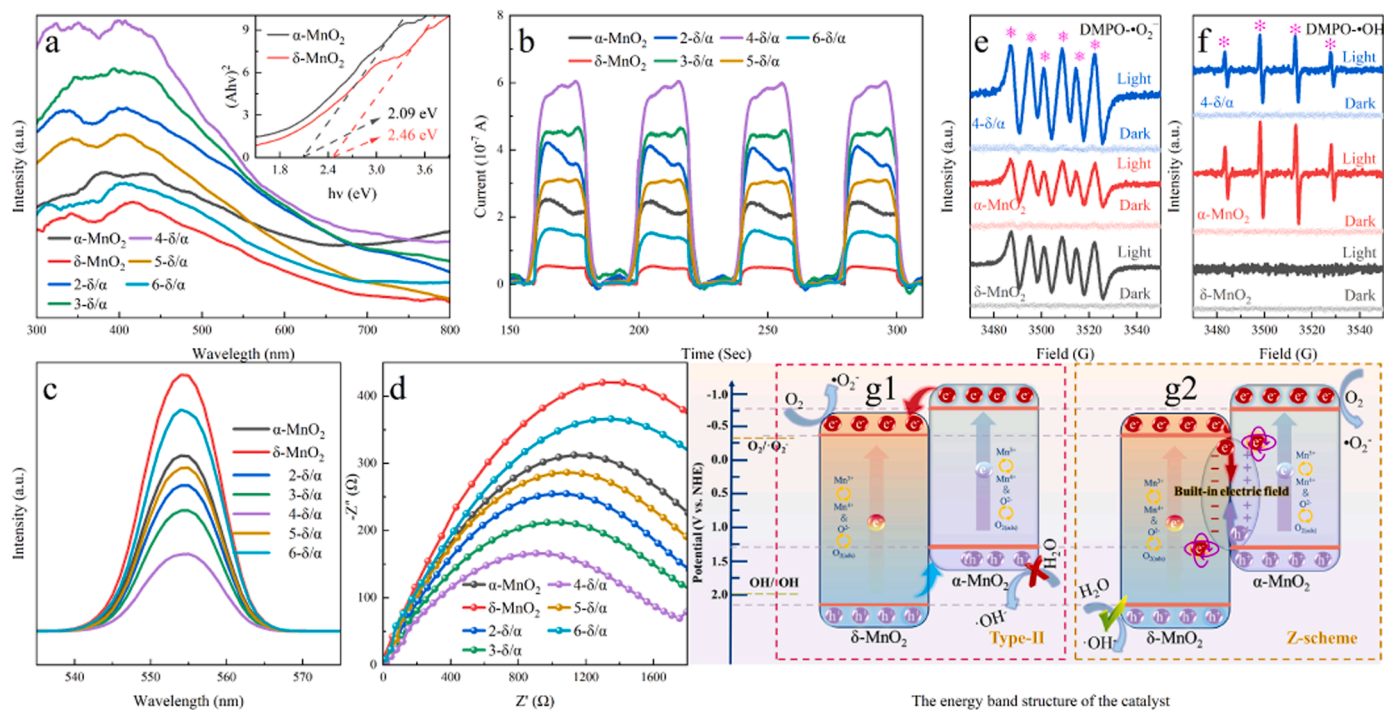


Fig. 6. (a) The UV-vis diffuse spectra and corresponding Tauc curves of $(\alpha h\nu)^2$ versus photon energy $h\nu$ for the direct band gaps of α - MnO_2 and δ - MnO_2 , (b) transient photocurrent response profiles, (c) photoluminescence spectra (PL), (d) EIS Nyquist plots, DMPO-EPR spin-trapping spectra of samples before and after light irradiation of (e) $DMPO \cdot O_2$ radical, (f) $DMPO \cdot OH$ radical, schematic diagram of electron transfer mode (g1) traditional type-II and (g2) Z-scheme electron transfer.

investigate the charge transport process, exhibits a comparable pattern to PL. The arc with the smallest radius of the 4- δ/α conveys the weakest charge transfer resistance [51].

ESR experiments were conducted in the DMPO system to elucidate potential active species and the reaction mechanism. The ESR results in Fig. 6e demonstrate that all catalysts exhibit a six-fold representative signal of $\bullet\text{O}^{2-}$ under light conditions (none in the absence of light). Additionally, the peak intensity of $\bullet\text{O}^{2-}$ ranks in the following order: 4- $\delta/\alpha > \alpha\text{-MnO}_2 > \delta\text{-MnO}_2$. The enhancement of $\bullet\text{O}^{2-}$ in 4- δ/α further indicates the efficient spatial separation of photogenerated e^-h^+ and sufficient $\bullet\text{O}^{2-}$ production. Fig. 6f shows that, under lightless conditions, the samples do not exhibit OH characteristic peaks in their respective signal profiles. For $\delta\text{-MnO}_2$ and 4- δ/α catalysts, typical quadruple signal peaks of $\bullet\text{OH}$ are detected under light irradiation. However, for $\alpha\text{-MnO}_2$, no characteristic peak is observed in both dark and light due to its low valence band (less than 1.99 eV), which is insufficient to produce $\bullet\text{OH}$. Interestingly, the signal intensity of OH in $\delta\text{-MnO}_2$ is greater than in 4- δ/α due to the higher proportion of $\delta\text{-MnO}_2$ in the pristine catalyst compared to the composite catalyst. Additionally, $\alpha\text{-MnO}_2$ lacks the capability to generate $\bullet\text{OH}$ [52]. The generation of $\bullet\text{OH}$ and the augmentation of $\bullet\text{O}^{2-}$ are mainly attributed to the triumphant fabrication of heterojunction catalysts based on homogeneous junction composites.

There are two classical electron transfer modes, namely traditional II-type (Fig. 6g1) and Z-type (Fig. 6g2) electron transfer structure. If the 4- δ/α catalyst is II-type structure, the electrons will transfer from the conduction band of $\alpha\text{-MnO}_2$ to that of $\delta\text{-MnO}_2$. Since the E_{CB} (-0.35 V) of $\delta\text{-MnO}_2$ is more negative than the potential of $\text{O}_2/\bullet\text{O}^{2-}$ (-0.33 V vs NHE), $\bullet\text{O}^{2-}$ can be normally generated. However, for the E_{VB} (1.26 V) of $\alpha\text{-MnO}_2$, the 4- δ/α composite cannot produce $\bullet\text{OH}$ due to its lower redox potential than $\text{H}_2\text{O}/\bullet\text{OH}$ (1.99 V for NHE). This result is inconsistent the EPR test results shown in Fig. 5d. This indicates that the 4- δ/α catalyst forms the Z-type structure, and the photogenerated hot electrons are transferred from the CB of $\delta\text{-MnO}_2$ to the VB of $\alpha\text{-MnO}_2$. These electrons combine with the holes on the valence band, thus creating effective spatial separation, which further improves the charge separation efficiency. Moreover, the built-in electric field formed by the homojunction greatly promotes the rapid transfer of photogenerated carriers.

3.4.3. Energy distribution and transfer laws for catalyst charges

In order to gain more insight into the surface charge energy distribution of the materials, the density of states of $\delta\text{-MnO}_2$, $\alpha\text{-MnO}_2$ and 4- δ/α catalysts was calculated using DFT. The Mn's projected density of states (PDOS) of continuously distributed on catalysts in Fig. 7a indicates that the sample has good electron transfer ability. In general, the activation ability of the pollutant and the intermediate is stronger when

the d-band center of the transition metal is closer to the Fermi level (0 eV), indicating a higher surface electron energy of the material [53]. The PDOS- calculated d-band center values of $\delta\text{-MnO}_2$, $\alpha\text{-MnO}_2$ and 4- δ/α are -0.90, -0.85 and -0.66 eV, respectively. This suggests that 4- δ/α has a stronger activation ability, which enhances the propane degradation performance in PTSCO system.

The generation mechanism and separation capacity of photo-generated carriers are important factors affecting the catalytic oxidation performance of PTSCO system. The electrostatic potential distribution of 4-a/b shows that there are a large number of electron-rich regions at the heterojunction interface (Fig. 7b), which greatly enhances the adsorption performance of propane at the interface. The distribution of HOMO and LUMO reveals the mechanism of separation for photogenerated e^-h^+ . The results indicate that the HOMO (Fig. S11a) and LUMO (Fig. S11b) in $\alpha\text{-MnO}_2$, $\delta\text{-MnO}_2$ are basically evenly distributed on each atom, which is unfavorable to the separation of photogenerated carriers [54]. However, the heterojunction structure significantly alters the charge distribution characteristics of the sample, resulting in a highly asymmetric on 4- δ/α . This greatly enhances the separation efficiency of photogenerated carriers on its surface. Furthermore, Fig. 7c shows the differential charge density diagrams of $\delta\text{-MnO}_2$ and $\alpha\text{-MnO}_2$. A clear electron-rich region is visible on the surface of $\alpha\text{-MnO}_2$, while $\delta\text{-MnO}_2$ has an electron-deficient region. This reconfirms the transfer of electrons from $\delta\text{-MnO}_2$ to $\alpha\text{-MnO}_2$ surface in the built-in electric field. This effectively inhibits the recombination of photogenerated carriers on the surface of 4- δ/α while maintaining high redox performance, which is also highly consistent with the PL results. Moreover, in our previous study, the enhancement of photothermal activity by defects was also proved by DFT calculations. The electronic defects caused by the surface defects of the catalyst are beneficial to the adsorption and electron transfer of the reactants. In addition, the band structure and work function calculation results indicate that the electrons surrounding the defect are more easily excited and participate in the reaction under light and heat. And electrons will flow to the lower side of the work function, resulting in electron enrichment at the defect. The results of the density of states (DOS) also indicate a reduction in the surface charge density of defect-rich MnO_2 , which greatly promotes the photothermal synergistic catalytic oxidation of propane[55].

3.5. Enhanced photothermal activity mechanism

3.5.1. in-situ DRIFTS for propane adsorption and oxidation

To further explore the mechanism of photothermal synergistic catalytic oxidation for propane in PTSCO system, the adsorption process of propane on $\alpha\text{-MnO}_2$ and 4- δ/α catalysts at 50°C are tracked by in-situ DRIFTS technology under the condition of 2500 ppm $\text{C}_3\text{H}_8 + \text{N}_2$ and

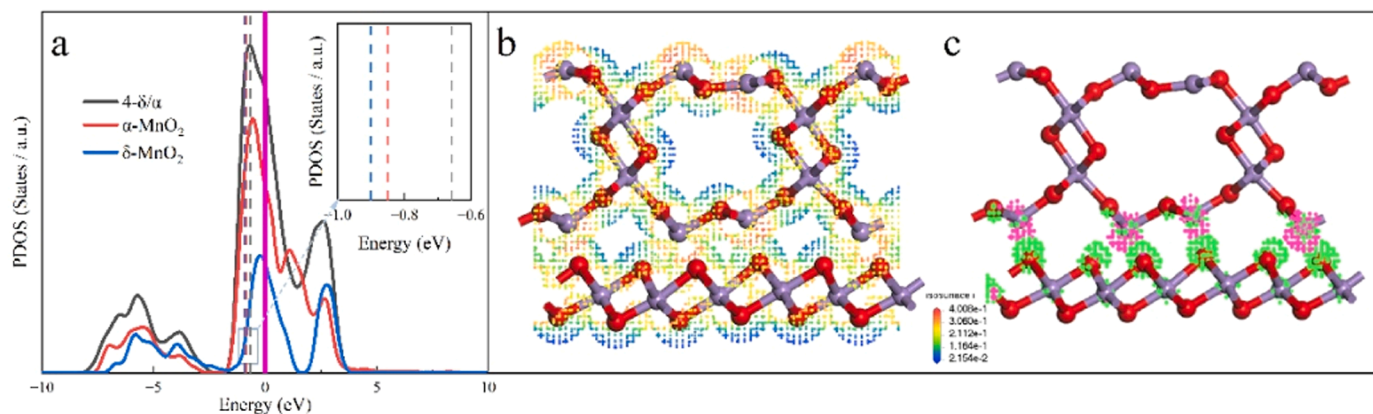


Fig. 7. (a) The Mn (PDOS) on $\alpha\text{-MnO}_2$, $\delta\text{-MnO}_2$ and 4- δ/α , (b) electrostatic potential distribution and (c) the differential charge density plot of 4- δ/α catalyst. The red ball is oxygen and purple ball represents manganese. The colors green and pink represent positive and negative isosurfaces, respectively. The isosurface value is $0.015 \text{ e}^- \text{Å}^{-3}$.

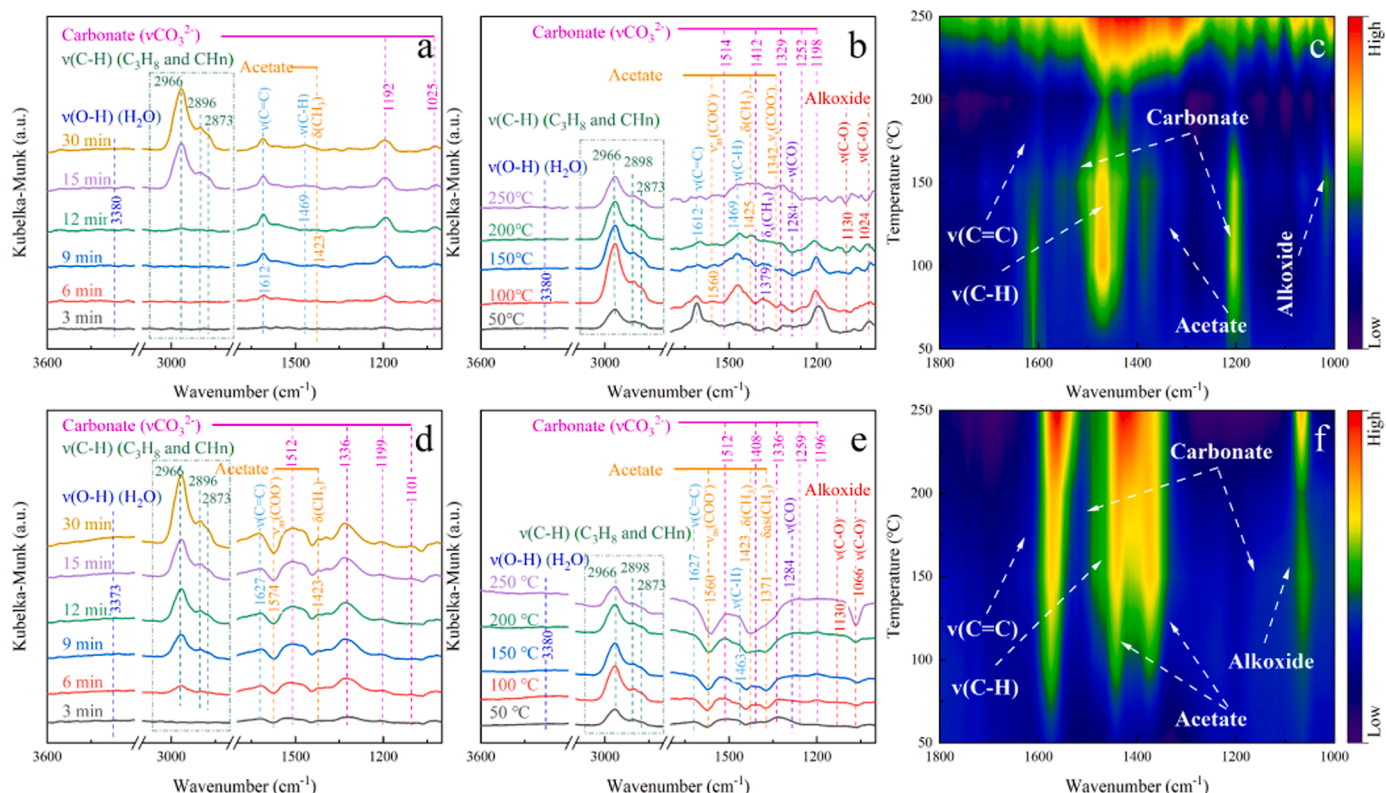


Fig. 8. *In situ* DRIFTS spectra of propane adsorption over (a) α -MnO₂ and (d) δ -MnO₂ catalyst at different time with 2500 ppm propane + N₂. *In situ* DRIFTS spectra of propane oxidation and the corresponding contour projection on (b, c) α -MnO₂ and (e, f) δ -MnO₂ catalyst at different temperature with 2500 ppm propane + air.

50 °C. As presented in Fig. 8, the strong peak at 2966 cm⁻¹ is attributed to adsorbed gaseous propane, while the bands at 2896 and 2873 cm⁻¹ are associated to the stretching vibration of CH_n (CH₂ or CH₃) species [56]. Additionally, a wide ν (O-H) stretching vibration belonging to hydroxyl or adsorbed water appears near 3380 cm⁻¹. Multiple characteristic peaks attributed to carbonate species (1025 and 1192 cm⁻¹), carboxylate species (1423 cm⁻¹) and propylene C-H (1469 cm⁻¹) and C = C (1612 cm⁻¹) are observed, and the majority of the peaks gradually increase and reach a stable level with the passage of reaction time. As the adsorption takes place in an oxygen-free environment, the emergence of intermediate products suggests that the surface active oxygen species or lattice oxygen of α -MnO₂ are involved in the oxidation of propane to some extent [57]. Obviously, the adsorption process of propane on 4- δ / α is similar to that of α -MnO₂ (Fig. 8d), but with more intermediates present. The spectra of species such as carbonates (1336 cm⁻¹ and 1512 cm⁻¹) and the asymmetric stretching vibration of carboxylate carbonyls (1574 cm⁻¹) show stronger peaks in 4- δ / α , indicating the presence of more reactive oxygen species. This confirms that 4- δ / α , with stronger acidity, has better adsorption performance than α -MnO₂. This confirms that 4- δ / α , which is more acidic, has better adsorption properties than α -MnO₂. Additionally, the adsorption equilibrium time of propane on B is 30 min, while it only needs 15 minutes on α -MnO₂, suggesting that catalyst 4- δ / α with heterojunction structure adsorbs propane more rapidly and dissociates propane better.

The in-situ DRIFT spectra of propane oxidation over α -MnO₂ and 4- δ / α were determined at specific temperatures after switching the feed gas to 2500 ppm C₃H₈ + air. During the reaction on sample α -MnO₂ (Fig. 8b, c), the peak intensities of C-H single-bond stretching vibrations of propane show an initial increase follow a decrease. Noticeably, more intermediates appear in the range of 1000–1700 cm⁻¹ (the peak intensity is increased by 4 times to better elucidate the intermediates). Briefly, for the catalytic oxidation of propane on α -MnO₂, bands of C-O single bonds belonging to the alcohol salt species in the range of

1000–1200 cm⁻¹ (1180 and 1040 cm⁻¹) are also detected [58]. In addition, the peaks attributed to carbonate stretching vibrations at 1198, 1252, 1329, 1412 and 1514 cm⁻¹, as well as asymmetric bending vibrations of (CH₃) species at 1425 cm⁻¹ are successfully identified. Moreover, symmetric stretching vibrations (Vs(COO)) and asymmetric stretching vibrations (Vas(COO)) corresponding to carboxylate/ester carbonyls are observed at 1342 and 1560 cm⁻¹ [59]. Fig. 8e, f demonstrate that catalyst 4- δ / α follows a propane degradation pathway similar to that of α -MnO₂, but with differences in the evolution of intermediates. During the reaction, the peak intensity of propane on 4- δ / α decreases more significantly than that of on α -MnO₂ catalyst (Fig. S12), indicating a faster reaction rate for propane on 4- δ / α catalyst. Additionally, the contents of alkoxides, carbonates, carboxylates, and propylene on sample 4- δ / α decreased sharply or were undetectable compared to sample α -MnO₂, indicating that sample 4- δ / α degraded propane more thoroughly and had stronger oxidation performance.

Additionally, 4- δ / α has the highest propane adsorption and oxidation capacity, as indicated by the adsorption energies of propane, water vapor and oxygen, and the dissociation energies of oxygen on δ -MnO₂, α -MnO₂ and 4- δ / α (Fig. S13a–S13d). Furthermore, the two degradation pathways simulated by DFT calculations reveal that the rate-determining step of propane dissociation on 4- δ / α catalysts requires less energy compare to α -MnO₂, regardless of the degradation pathway (Fig. S14).

3.5.2. Photothermal synergistic catalytic oxidation mechanism

The results indicate that the difference in propane catalytic oxidation activity between the PTSCO system and TCO system is mainly due to the introduction of light. Propane degradation in the TCO system primarily relies on the cyclic supply of reactive oxygen species (ROS) and electrons of the material, as shown in Fig. 9. Pathway ① demonstrates that reactive oxygen species oxidize the adsorbed activated propane molecules, accompanied by the regeneration of oxygen vacancies. In the

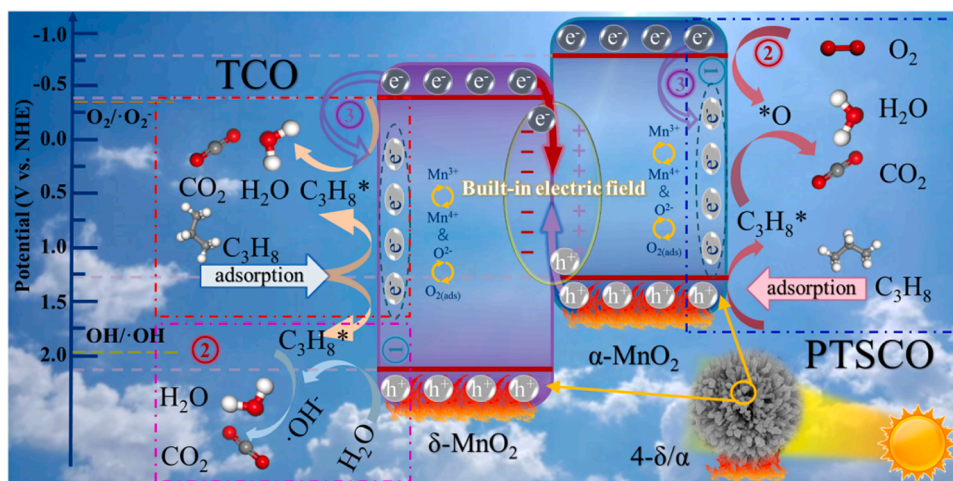


Fig. 9. The synergy mechanism of propane degradation in PTSCO system. The ball colors represent oxygen (red), manganese (purple), hydrogen (white), and carbon (gray).

PTSCO system, the homojunction structure of the 4- δ/α catalyst results in a higher E_{VB} side (2.11 V) than the redox potential of the hydroxyl group ($H_2O/\bullet OH$: -1.99 V vs NHE), and a lower E_{CB} side (-0.83 V) than the redox potential of the oxygen ($O_2/\bullet O_2^-$: -0.33 V vs NHE). Therefore, the photogenerated carriers can react with oxygen and water in the product or raw material through pathway ② to generate $\bullet O_2^-$ and $\bullet OH$ with higher redox properties, which can further facilitate the catalytic oxidation process on the surface. These free radicals can rapidly convert the intermediates, leading to the accelerated release of active sites and ultimately promoting the rate of oxidation reaction. Moreover, the rapid transfer of electrons caused by the built-in electric field further accelerates the reaction process of the above process.

Additionally, it is important to note that high temperatures can accelerate motion activation of molecular, facilitate the production and migration of photogenerated e^-h^+ and improve mass transfer efficiency. Some of these photogenerated electrons interact with oxygen to generate ROS, while others are directly involved in the propane oxidation in the TCO system. This improves the ability to generate and separate photogenerated e^-h^+ pairs (③). As a result, at the same temperature and light intensity, the T_{50} and T_{90} for propane oxidation in the PTSCO system decreased considerably. Furthermore, in the case of the PTSCO system, an increase in temperature promotes the desorption or conversion of products on the catalyst, leading to the timely release of active sites and an improvement in the material's long-term performance.

4. Conclusion

In conclusion, a series of δ - and α -phase MnO_2 homojunction catalysts ($x\text{-}\delta/\alpha$) with different ratios were synthesized by a simple hydrothermal stirring method and used for the complete catalytic oxidation of propane in the PTSCO system. Under the given conditions of the propane concentration of 2500 ppm, light intensity of $720\text{ mW}\cdot\text{cm}^{-2}$, and WHSV of $30000\text{ mL}\cdot\text{g}_{\text{cat}}^{-1}\cdot\text{h}^{-1}$, 4- δ/α exhibited the highest propane degradation activity ($T_{90} = 198^\circ\text{C}$, $E_a = 25.36\text{ kJ}\cdot\text{mol}^{-1}$ and $\text{TOF} = 5.36 \times 10^{-3}$). The catalyst also exhibited good water resistance, long-term stability and recyclability. The analysis of the characteristics and the DFT calculation demonstrate that the band structure of 4- δ/α is appropriate, resulting in the formation of a built-in electric field with the faster transfer of electron at the homojunction interface. This electric field mediates the Z-type electron transport pathway, effectively suppressing the recombination of photogenerated carriers and maintaining the high redox performance of the catalyst. Furthermore, the introduction of light stimulates the production of reactive oxygen species and accelerates the

degradation of intermediates. In summary, this study proposes a novel approach for designing and synthesizing high-efficiency photothermal homojunction catalysts, which advances the development of low-energy and high-efficiency technology for treating VOCs.

CRedit authorship contribution statement

Yuxi Bi: Writing – review & editing, Writing – original draft, Methodology, Investigation, Formal analysis, Conceptualization. **Guoyang Ji:** Validation, Investigation, Formal analysis, Data curation. **Yadi Wang:** Validation, Data curation. **Yuekun Jing:** Validation, Data curation. **Guofei Jiang:** Validation, Methodology, Conceptualization. **Chao Feng:** Methodology, Funding acquisition, Conceptualization. **Fang Liu:** Writing – review & editing, Supervision, Project administration, Funding acquisition. **Yunqi Liu:** Resources, Project administration, Conceptualization. **Huazhen Chang:** Project administration, Conceptualization.

Declaration of Competing Interest

The authors declare that they have no known competing financial interests or personal relationships that could have appeared to influence the work reported in this paper.

Data availability

Data will be made available on request.

Acknowledgments

This work was financially supported by the CNPC safety and environmental protection key technology research and promotion project (2017D-4613), Sub project of National Science and Technology major project (2016ZX05040-003) and Qingdao Postdoctoral Program Funding (QDBSH202202039), China Postdoctoral Science Foundation (2023M733612) and Qingdao Natural Science Foundation (23-2-1-14-zyyd-jch).

Appendix A. Supporting information

Supplementary data associated with this article can be found in the online version at [doi:10.1016/j.apcatb.2024.123920](https://doi.org/10.1016/j.apcatb.2024.123920).

References

- [1] Y. Zhang, Y. Wang, R. Xie, H. Huang, M.K.H. Leung, J. Li, D.Y.C. Leung, Photocatalytic oxidation for volatile organic compounds elimination: from fundamental research to practical applications, *Environ. Sci. Technol.* 56 (2022) 16582–16601.
- [2] S. Jiang, C. Li, Y. Muhammad, Y. Tang, R. Wang, J. Li, J. Li, Z. Zhao, Z. Zhao, Solvent-induced fabrication of Cu/MnOx nanosheets with abundant oxygen vacancies for efficient and long-lasting photothermal catalytic degradation of humid toluene vapor, *Appl. Catal. B: Environ.* 328 (2023) 122509.
- [3] S. Mo, X. Zhao, L. Huang, J. Zhou, S. Li, R. Peng, Z. Tu, L. Liao, Q. Xie, Y. Chen, Y. Zhang, D. Ye, Uncovering the role of unsaturated coordination defects in manganese oxides for concentrated solar-heating photothermal OVOCs oxidation: experimental and DFT explorations, *Appl. Catal. B: Environ.* 342 (2024) 123435.
- [4] Y. Yang, S. Zhao, L. Cui, F. Bi, Y. Zhang, N. Liu, Y. Wang, F. Liu, C. He, X. Zhang, Recent advancement and future challenges of photothermal catalysis for VOCs elimination: from catalyst design to applications, *Green Energy Environ.* 8 (2023) 654–672.
- [5] K. Zhang, H. Ding, W. Pan, X. Mu, K. Qiu, J. Ma, Y. Zhao, J. Song, Z. Zhang, Research progress of a composite metal oxide catalyst for VOC degradation, *Environ. Sci. Technol.* 56 (2022) 9220–9236.
- [6] M. Zhang, X. Sui, X. Zhang, M. Niu, C. Li, H. Wan, Z. Qiao, H. Xie, X. Li, Multi-defects engineering of NiCo₂O₄ for catalytic propane oxidation, *Appl. Surf. Sci.* 600 (2022) 154040.
- [7] Y. Wang, S. Aghamohammadi, D. Li, K. Li, R. Farrauto, Structure dependence of Nb₂O₅-X supported manganese oxide for catalytic oxidation of propane: enhanced oxidation activity for MnO_x on a low surface area Nb₂O₅-X, *Appl. Catal. B: Environ.* 244 (2019) 438–447.
- [8] W. Tan, S. Xie, Y. Cai, H. Yu, K. Ye, M. Wang, W. Diao, L. Ma, S.N. Ehrlich, F. Gao, L. Dong, F. Liu, Surface lattice-embedded Pt single-atom catalyst on ceria-zirconia with superior catalytic performance for propane oxidation, *Environ. Sci. Technol.* 57 (2023) 12501–12512.
- [9] W. Zhang, J.L. Valverde, A. Giroir-Fendler, Co₃O₄-based catalysts for propane total oxidation: a state-of-the-art minireview, *Appl. Catal. B: Environ.* 337 (2023) 122908.
- [10] G. Li, K. He, F. Zhang, G. Jiang, Z. Zhao, Z. Zhang, J. Cheng, Z. Hao, Defect enhanced CoMnNiO_x catalysts derived from spent ternary lithium-ion batteries for low-temperature propane oxidation, *Appl. Catal. B: Environ.* 309 (2022) 121231.
- [11] X. Min, M. Guo, L. Liu, L. Li, J. Gu, J. Liang, C. Chen, K. Li, J. Jia, T. Sun, Synthesis of Mn₂O₃ derived from spent lithium-ion batteries via advanced oxidation and its application in VOCs oxidation, *J. Hazard. Mater.* 406 (2021) 124743.
- [12] R. Rajesh, S. Lingalwar, P. Challa, P. Balla, S. B. V.P. Sruthi, S. Kim, S. Senthilkumar, V. Perupogu, Low-temperature total oxidation of propane using silver-decorated MnO₂ nanorods, *ACS Appl. Nano Mater.* 6 (2023) 12258–12270.
- [13] R. Yang, Y. Fan, R. Ye, Y. Tang, X. Cao, Z. Yin, Z. Zeng, MnO₂-based materials for environmental applications, *Adv. Mater.* 33 (2021) 2004862.
- [14] Z. Pan, M. Zhao, H. Zhuzhang, G. Zhang, M. Anpo, X. Wang, Gradient Zn-doped poly heptazine imides integrated with a van der Waals homojunction boosting visible light-driven water oxidation activities, *ACS Catal.* 11 (2021) 13463–13471.
- [15] H. Dong, X. Zhang, J. Li, P. Zhou, S. Yu, N. Song, C. Liu, G. Che, C. Li, Construction of morphology-controlled nonmetal 2D/3D homojunction towards enhancing photocatalytic activity and mechanism insight, *Appl. Catal. B: Environ.* 263 (2020) 118270.
- [16] Z. Ai, K. Zhang, D. Shi, B. Chang, Y. Shao, L. Zhang, Y. Wu, X. Hao, Band-matching transformation between CdS and BCNTs with tunable p-n homojunction for enhanced photocatalytic pure water splitting, *Nano Energy* 69 (2020) 104408.
- [17] J. Lyu, J. Gao, M. Zhang, Q. Fu, L. Sun, S. Hu, J. Zhong, S. Wang, J. Li, Construction of homojunction-adsorption layer on anatase TiO₂ to improve photocatalytic mineralization of volatile organic compounds, *Appl. Catal. B: Environ.* 202 (2017) 664–670.
- [18] N. Huang, Z. Qu, C. Dong, Y. Qin, X. Duan, Superior performance of α/β -MnO₂ for the toluene oxidation: active interface and oxygen vacancy, *Appl. Catal. A: Gen.* 560 (2018) 195–205.
- [19] Y. Shen, S. Liu, L. Lu, C. Zhu, Q. Fang, R. Liu, Z. He, Y. Li, S. Song, Photocatalytic degradation of Toluene by a TiO₂ p-n homojunction nanostructure, *ACS Appl. Nano Mater.* 5 (2022) 18612–18621.
- [20] L. Liao, X. Ding, J. Li, L. Huang, M. Zhang, Y. Fan, X. Zhou, Y. Zhang, S. Mo, Q. Xie, D. Ye, Constructing MOFs-derived Co₃O₄ microsphere with atomic p-n homojunction as an efficient photothermal catalyst for boosting ethyl acetate oxidation under light irradiation, *Sep. Purif. Technol.* 309 (2023) 122939.
- [21] Z. Ma, G. Shao, Y. Fan, G. Wang, J. Song, D. Shen, Construction of hierarchical α -MnO₂ nanowires/ultrathin δ -MnO₂ nanosheets core-shell nanostructure with excellent cycling stability for high-power asymmetric supercapacitor electrodes, *ACS Appl. Mater. Interfaces* 8 (2016) 9050–9058.
- [22] J. Cao, Q. Mao, L. Shi, Y. Qian, Fabrication of gamma-MnO₂/alpha-MnO₂ hollow core/shell structures and their application to water treatment, *J. Mater. Chem.* 40 (2011) 16210–16215.
- [23] T. Su, B. Zhao, B. Fan, H. Li, R. Zhang, Enhanced microwave absorption properties of novel hierarchical core-shell δ/α MnO₂ composites, *J. Solid State Chem.* 273 (2019) 192–198.
- [24] M. Dilla, A. Mateblowski, S. Ristig, J. Strunk, Photocatalytic CO₂ reduction under continuous flow high-purity conditions: influence of light intensity and H₂O concentration, *ChemCatChem* 9 (2017) 4345–4352.
- [25] X. Yu, J. Deng, Y. Liu, L. Jing, R. Gao, Z. Hou, Z. Zhang, H. Dai, Enhanced water resistance and catalytic performance of Ru/TiO₂ by regulating Brønsted acid and oxygen vacancy for the oxidative removal of 1,2-dichloroethane and toluene, *Environ. Sci. Technol.* 56 (2022) 11739–11749.
- [26] L. Kang, X. Liu, A. Wang, L. Li, Y. Ren, X. Li, X. Pan, Y. Li, X. Zong, H. Liu, A. I. Frenkel, T. Zhang, Photo-thermo catalytic oxidation over a TiO₂-WO₃-supported platinum catalyst, *Angew. Chem. Int. Ed.* 59 (2020) 12909–12916.
- [27] K. Zeng, X. Li, C. Wang, Z. Wang, P. Guo, J. Yu, C. Zhang, X. Zhao, Three-dimensionally macroporous MnZrO_x catalysts for propane combustion: synergistic structure and doping effects on physicochemical and catalytic properties, *J. Colloid Interface Sci.* 572 (2020) 281–296.
- [28] W. Liu, W. Xiang, X. Chen, Z. Song, C. Gao, N. Tsubaki, X. Zhang, A novel strategy to adjust the oxygen vacancy of CuO/MnO₂ catalysts toward the catalytic oxidation of toluene, *Fuel* 312 (2022) 122975.
- [29] J. Jia, P. Zhang, L. Chen, Catalytic decomposition of gaseous ozone over manganese dioxides with different crystal structures, *Appl. Catal. B: Environ.* 189 (2016) 210–218.
- [30] S. Wang, J. Xie, Z. Deng, M. Wu, F. Wang, HCHO oxidation over the δ -MnO₂ catalyst: enhancing oxidative activities of surface lattice oxygen and surface adsorbed oxygen by weakening Mn-O bond, *Fuel* 344 (2023) 128141.
- [31] S. Rong, P. Zhang, F. Liu, Y. Yang, Engineering crystal facet of α -MnO₂ nanowire for highly efficient catalytic oxidation of carcinogenic airborne formaldehyde, *ACS Catal.* 8 (2018) 3435–3446.
- [32] L. Chen, Y. Liu, X. Fang, Y. Cheng, Simple strategy for the construction of oxygen vacancies on α -MnO₂ catalyst to improve toluene catalytic oxidation, *J. Hazard. Mater.* 409 (2021) 125020.
- [33] S. Zhao, Y. Yang, F. Bi, Y. Chen, M. Wu, X. Zhang, G. Wang, Oxygen vacancies in the catalyst: Efficient degradation of gaseous pollutants, *Chem. Eng. J.* 454 (2023) 140376.
- [34] J. Wang, Z. Hou, X. Liu, S. Wang, S. Yao, Y. Yao, D. Wang, X. Gao, H. Zhang, Z. Tang, Y. Liu, K. Nie, J. Xie, Z. Yang, Y.-M. Yan, Boosted sodium ion storage performance in MnO₂: understanding the bond angle-mediated orbital overlap in MnO₆ units for fast charge transfer, *J. Energy Chem.* 87 (2023) 295–303.
- [35] M.T.N. Dinh, C.C. Nguyen, M.D. Phan, M.K. Duong, P.H.D. Nguyen, C. Lancelot, D. L. Nguyen, Novel cryptomelane nanosheets for the superior catalytic combustion of oxygenated volatile organic compounds, *J. Hazard. Mater.* 417 (2021) 126111.
- [36] W. Lv, J. Meng, Y. Li, W. Yang, Y. Tian, X. Lyu, C. Duan, X. Ma, Y. Wu, Inexpensive and eco-friendly nanostructured birnessite-type δ -MnO₂: a design strategy from oxygen defect engineering and K⁺ pre-intercalation, *Nano Energy* 98 (2022) 107274.
- [37] Y. Shi, W. Su, L. Kong, J. Wang, P. Lv, J. Hao, X. Gao, G. Yu, The homojunction formed by h-In₂O₃(110) and c-In₂O₃(440) promotes carbon dioxide hydrogenation to methanol on graphene oxide modified In₂O₃, *J. Colloid Interface Sci.* 623 (2022) 1048–1062.
- [38] H. Zhang, Y. Jia, Y. Li, L. Wang, C. Ouyang, S. Zhong, Ni/Ce co-doping δ -MnO₂ nanosheets with oxygen vacancy for enhanced electrocatalytic oxygen evolution reaction, *Int. J. Hydrog. Energy* 48 (2023) 2652–2662.
- [39] H. Liu, W. Jia, X. Yu, X. Tang, X. Zeng, Y. Sun, T. Lei, H. Fang, T. Li, L. Lin, Vitamin C-assisted synthesized Mn-Co oxides with improved oxygen vacancy concentration: boosting lattice oxygen activity for the air-oxidation of 5-(hydroxymethyl) furfural, *ACS Catal.* 11 (2021) 7828–7844.
- [40] S. Wu, H. Liu, Z. Huang, H. Xu, W. Shen, O-vacancy-rich porous MnO₂ nanosheets as highly efficient catalysts for propane catalytic oxidation, *Appl. Catal. B: Environ.* 312 (2022) 121387.
- [41] Y. Yang, S. Zhao, F. Bi, J. Chen, Y. Wang, L. Cui, J. Xu, X. Zhang, Highly efficient photothermal catalysis of toluene over Co₃O₄/TiO₂ p-n heterojunction: the crucial roles of interface defects and band structure, *Appl. Catal. B: Environ.* 315 (2022) 121550.
- [42] C. Feng, Q. Gao, G. Xiong, Y. Chen, Y. Pan, Z. Fei, Y. Li, Y. Lu, C. Liu, Y. Liu, Defect engineering technique for the fabrication of LaCoO₃ perovskite catalyst via urea treatment for total oxidation of propane, *Appl. Catal. B: Environ.* 304 (2022) 121005.
- [43] H. Zhang, S. Sui, X. Zheng, R. Cao, P. Zhang, One-pot synthesis of atomically dispersed Pt on MnO₂ for efficient catalytic decomposition of toluene at low temperatures, *Appl. Catal. B: Environ.* 257 (2019) 117878.
- [44] X. Chen, S. Zhang, W. Liu, R. Cui, S. Liu, Y. Feng, X. Zhang, Efficient toluene low-temperature elimination over manganese oxides: unveiling the decisive role of lattice oxygen, *Appl. Organomet. Chem.* 37 (2023) e7054.
- [45] S. Wu, H. Liu, Z. Huang, H. Xu, W. Shen, Mn_{1.2}Zr_xO_y mixed oxides with abundant oxygen vacancies for propane catalytic oxidation: insights into the contribution of Zr doping, *Chem. Eng. J.* 452 (2023) 139341.
- [46] Y. Lu, Y. Wang, Q. Tang, Q. Cao, W. Fang, Synergy in Sn-Mn oxide boosting the hydrogenation catalysis of supported Pt nanoparticles for selective conversion of levulinic acid, *Appl. Catal. B: Environ.* 300 (2022) 120746.
- [47] G. Zhang, W. Han, H. Zhao, L. Zong, Z. Tang, Solvothermal synthesis of well-designed ceria-tin-titanium catalysts with enhanced catalytic performance for wide temperature NH₃-SCR reaction, *Appl. Catal. B: Environ.* 226 (2018) 117–126.
- [48] H. Zhou, F. Zhang, K. Ji, J. Gao, P. Liu, K. Zhang, S. Wu, Relationship between acidity and activity on propane conversion over metal-modified HZSM-5 catalysts, *Catalysts* 11 (2021) 1138.
- [49] Y. Jian, M. Tian, C. He, J. Xiong, Z. Jiang, H. Jin, L. Zheng, R. Albilal, J. Shi, Efficient propane low-temperature destruction by Co₃O₄ crystal facets engineering: unveiling the decisive role of lattice and oxygen defects and surface acid-base pairs, *Appl. Catal. B: Environ.* 283 (2021) 119657.
- [50] F. Chang, W. Yan, X. Wang, S. Peng, S. Li, X. Hu, Strengthened photocatalytic removal of bisphenol A by robust 3D hierarchical n-p heterojunctions Bi₄O₅Br₂-MnO₂ via boosting oxidative radicals generation, *Chem. Eng. J.* 428 (2022) 131223.

- [51] X. Li, G. Fang, X. Qian, Q. Tian, Z-scheme heterojunction of low conduction band potential MnO_2 and biochar-based g- C_3N_4 for efficient formaldehyde degradation, *Chem. Eng. J.* 428 (2022) 131052.
- [52] Y. Liu, M. Pei, H. Liang, X. Wu, B. Li, Z. Si, F. Kang, Rational design and preparation of Pt-LDH/ CeO_2 catalyst for high-efficiency photothermal catalytic oxidation of toluene, *ACS Appl. Mater. Interfaces* 14 (2022) 36633–36643.
- [53] C. Feng, C. Chen, G. Xiong, D. Yang, Z. Wang, Y. Pan, Z. Fei, Y. Lu, Y. Liu, R. Zhang, Cr-doping regulates Mn_3O_4 spinel structure for efficient total oxidation of propane: Structural effects and reaction mechanism determination, *Appl. Catal. B: Environ.* 328 (2023) 122528.
- [54] T. Kamachi, T. Tatsumi, T. Toyao, Y. Hinuma, Z. Maeno, S. Takakusagi, S. Furukawa, I. Takigawa, K.-I. Shimizu, Linear correlations between adsorption energies and HOMO levels for the adsorption of small molecules on TiO_2 surfaces, *The, J. Phys. Chem. C* 123 (2019) 20988–20997.
- [55] C. Feng, Y. Bi, C. Chen, S. Li, Z. Wang, H. Xin, Y. Pan, F. Liu, Y. Lu, Y. Liu, R. Zhang, X. Li, Urea- H_2O_2 defect engineering of $\delta\text{-MnO}_2$ for propane photothermal oxidation: Structure-activity relationship and synergetic mechanism determination, *J. Colloid Interface Sci.* 641 (2023) 48–58.
- [56] G. Li, N. Li, Y. Sun, Y. Qu, Z. Jiang, Z. Zhao, Z. Zhang, J. Cheng, Z. Hao, Efficient defect engineering in Co-Mn binary oxides for low-temperature propane oxidation, *Appl. Catal. B: Environ.* 282 (2021) 119512.
- [57] K. Zha, H. Liu, L. Xue, Z. Huang, H. Xu, W. Shen, Co_3O_4 nanoparticle-decorated SiO_2 nanotube catalysts for propane oxidation, *ACS Appl. Nano Mater.* 4 (2021) 8937–8949.
- [58] X. Lai, X. Zhou, H. Zhang, X. Jiang, T. Lin, Y. Chen, Toluene oxidation over monolithic $\text{MnO}_x/\text{La-Al}_2\text{O}_3$ catalyst prepared by a CTAB-assisted impregnation method, *Appl. Surf. Sci.* 526 (2020) 146714.
- [59] W. Liu, S. Yang, Q. Zhang, T. He, Y. Luo, J. Tao, D. Wu, H. Peng, Insights into flower-like Al_2O_3 spheres with rich unsaturated pentacoordinate Al^{3+} sites stabilizing Ru-CeOx for propane total oxidation, *Appl. Catal. B: Environ.* 292 (2021) 120171.